

Growth of the MRI in Accretion Discs – the Influence of Radiation Transport

M. Flaig,¹ R. Kissmann,¹ W. Kley,¹

¹ *Institut für Astronomie & Astrophysik, Universität Tübingen, Auf der Morgenstelle 10, 72076 Tübingen, Germany*

Accepted ???. Received ??; in original form ??

ABSTRACT

In this paper we investigate the influence of radiative transport on the growth of the magnetorotational instability (MRI) in accretion discs. The analysis is performed by use of analytical and numerical means. We provide a general dispersion relation together with the corresponding eigenfunctions describing the growth rates of small disturbances on a homogeneous background shear flow. The dispersion relation includes compressibility and radiative effects in the flux-limited diffusion approximation. By introducing an effective speed of sound, all the effects of radiation transport can be subsumed into one single parameter. It can be shown that the growth rates of the vertical modes – which are the fastest growing ones – are reduced by radiative transport. For the case of non-vertical modes, the growth rates may instead be enhanced. We quantify the effects of compressibility and radiative diffusion on the growth rates for the gas-pressure dominated case. The analytical discussion is supplemented by numerical simulations, which are also used for a first investigation of the non-linear stage of the MRI in gas-pressure dominated accretion discs with radiation transport included.

Key words: accretion, accretion discs – instabilities – magnetic fields – MHD – radiative transfer

1 INTRODUCTION

Accretion discs are believed to be present in a variety of astrophysical objects, namely active galactic nuclei, binary X-ray sources, cataclysmic variables and protostellar systems. The classical problem in the theory of accretion discs is why they are accreting, or, stated in other words, what is the mechanism which transports angular momentum outwards so that matter can spiral inwards? It cannot be ordinary molecular viscosity because it is several orders of magnitude too small to account for the observed accretion rates (Pringle 1981; Balbus 2003). In order to resolve this discrepancy, Shakura & Syunyaev (1973) introduced the phenomenological α -disc model where a large kinematic viscosity associated with turbulent motions in the disc is thought to drive outward angular momentum transport. What mechanism would make the discs turbulent, however, still remains a matter of debate. It is well known that in general shear flows are subject to nonlinear hydrodynamical instabilities, but it seems that a compelling case for hydrodynamical turbulence has not been made yet. In fact, the assumption that Keplerian discs are hydrodynamically unstable can be challenged both on analytical and numerical grounds (see, e.g., Hawley et al. 1999; Balbus & Hawley 2006). Since most accretion discs consist of ionised gas, it is thus only logical to focus on magnetohydrodynamical instabilities instead.

Nowadays it is the magnetorotational instability (Balbus & Hawley 1991, hereafter BH) that appears to be the most promising candidate. The instability is local, linear, powerful (the growth rates being of the order of the orbital period), and it exists even if the initial magnetic field is very weak. Both three-dimensional local shearing-box (Hawley et al. 1995; Brandenburg et al. 1995) and global disc simulations (Armitage 1998; Hawley 2000; Fromang & Nelson 2006) show that the resulting turbulence indeed transports significant amounts of angular momentum outwards, leading to values of the α -parameter that are in the range of $\alpha \sim 10^{-3} \dots 10^{-2}$, depending especially on the initial magnetic field configuration. When compared to observations, it seems that numerical simulations generally tend to yield α values that are too small, possibly due to numerical effects (King et al. 2007). The situation now looks rather complicated, since it has turned out that α does not only depend on physical parameters such as viscosity and resistivity, but also on details of the numerical setup, namely the numerical dissipation and resolution (Pessah et al. 2007; Fromang & Papaloizou 2007). Therefore it is very important to further investigate and to quantify the impact of the various physical and numerical parameters on the MRI-induced turbulent transport.

Despite the huge amount of numerical and analytical work that has been devoted to exploring the MRI in accre-

tion discs, comparatively little attention has been paid to the issue of radiation transport. Especially when it comes to simulations which are global in nature or at least include vertical stratification, there are relatively few works that include radiation transport (like Turner et. al. 2003, Turner 2004 for the radiation pressure-dominated case, Krolik et. al. 2007, Blaes et. al. 2007 for a disc with comparable radiation and gas pressure, and Hirose et. al. 2006 for the gas-pressure dominated case). Instead usually an isothermal equation of state is used (as, for example, in the works of Miller & Stone 2000; Papaloizou & Nelson 2003; Fromang & Nelson 2006). Yet from an isothermal model it is not possible to derive the true temperature profile, nor can one be sure that the resulting vertical structure is correct. If, on the other hand, one chooses an adiabatic equation of state, but does not include cooling, then the temperature in the disc will rise quite rapidly due to turbulent heating, which is also not very realistic. Only by including radiative transfer can we hope to model the energetics of MRI-generated turbulence correctly and achieve a quasi-steady turbulent state. In this work, we assume that the heat generated by the turbulence is transported by radiative diffusion.

Yet another point is, that incorporating radiative diffusion might well yield unexpected consequences. For example it has turned out recently that the migration of planets in a protoplanetary disc is significantly influenced by radiative effects (see, e.g., Kley & Crida 2008). It is not unreasonable to expect that radiative diffusion might have other important influences, for example when considering the growth of planetesimals out of dust in a turbulent disc (this has been pointed out recently in Brandenburg 2008). For these reasons, including radiation transport should be considered imperative on the road towards building more realistic models of accretion discs.

The plan of our paper is as follows: In Sec. 2 we derive the dispersion relation for axisymmetric MRI modes in a radiative, gas-pressure dominated accretion disc in the flux-limited diffusion approximation and calculate the corresponding eigenfunctions and MRI growth rates. In Sec. 3 we describe numerical simulations of single MRI modes using two different numerical schemes and demonstrate their excellent agreement with the analytical prediction. We also investigate the dependence of the saturation level of the MRI on the strength of radiative diffusion in a series of 3D local shearing box simulations. We conclude in Sec. 4, by discussing some consequences of our analysis and providing an outlook for further research. In the appendix we relax the assumption that gas pressure dominates radiation pressure and provide a general dispersion relation, including both the radiation dominated and the gas-pressure dominated case.

2 LINEAR ANALYSIS

2.1 Dispersion relation

We begin our analysis by deriving the MRI dispersion relation with radiation transport included in the one-temperature flux-limited diffusion approximation (see Levermore & Pomraning 1981). This means we assume that gas and radiation are at the same temperature and that the radiation energy is small compared to the internal energy of the gas, i.e. the disc is gas-pressure dominated.

As our starting point we take the equations of ideal magnetohydrodynamics, namely the continuity equation

$$\frac{\partial \rho}{\partial t} + \nabla \cdot (\rho \mathbf{v}) = 0, \quad (1a)$$

the equation of motion

$$\frac{\partial \mathbf{v}}{\partial t} + \mathbf{v} \cdot \nabla \mathbf{v} + \frac{1}{\rho} \nabla \left(p + \frac{B^2}{2\mu_0} \right) - \frac{\mathbf{B} \cdot \nabla \mathbf{B}}{\mu_0 \rho} + \nabla \Phi = 0, \quad (1b)$$

and the induction equation

$$\frac{\partial \mathbf{B}}{\partial t} = \nabla \times (\mathbf{v} \times \mathbf{B}). \quad (1c)$$

In Eq. (1b), Φ denotes the static gravitational potential of the central object. It vanishes when linearising the above equations, so we do not need to specify it. The other symbols have their usual meaning.

In order to perform a local stability analysis, we consider a patch of an accretion disc that is small enough so that the background density ρ , pressure p and magnetic field $\mathbf{B} = B_\phi \hat{\phi} + B_z \hat{z}$ can be taken constant. We do not include a radial component in the magnetic field; otherwise the background solution would not be time independent because an initially radial field would be sheared into a time-dependent azimuthal field. For a Keplerian disc, the background flow is locally $\mathbf{v} = -\frac{3}{2}\Omega r \hat{\phi}$, with Ω the angular orbital frequency. We impose plane-wave axisymmetric perturbations $\delta\rho, \delta\mathbf{v}, \delta\mathbf{B}, \delta p$ proportional to $\exp[i(k_r r + k_z z) + \sigma t]$, yielding the following linearised equations:

$$\sigma \delta\rho = -\rho \mathbf{k} \cdot \delta\mathbf{v}, \quad (2a)$$

$$\sigma \delta\mathbf{v} - \frac{3}{2}\Omega \delta v_r \hat{\phi} + \frac{i\mathbf{k}}{\rho} \cdot \left(C_{\text{eff}}^2 \delta\rho + \frac{\delta\mathbf{B} \cdot \mathbf{B}}{\mu_0} \right) - \frac{ik_z B_z}{\mu_0 \rho} \delta\mathbf{B} + 2\Omega \hat{z} \times \delta\mathbf{v} = 0, \quad (2b)$$

$$\sigma \delta\mathbf{B} = -i\mathbf{k} \cdot \delta\mathbf{v} \mathbf{B} + ik_z B_z \left(\delta\mathbf{v} - \frac{3\Omega}{2\sigma} \delta v_r \hat{\phi} \right); \quad (2c)$$

where we have introduced the *effective sound speed* C_{eff} via the definition $C_{\text{eff}}^2 \equiv \delta p / \delta\rho$. Note that Eq. (2c) ensures that the divergence-free constraint $\mathbf{k} \cdot \delta\mathbf{B} = 0$ be satisfied.

After eliminating $\delta\rho$ and $\delta\mathbf{B}$ from the linearised momentum equation (2b) by the use of (2a) and (2c), the remaining system of three equations can be readily solved. By defining a wavenumber K via

$$K \delta v_r \equiv \mathbf{k} \cdot \delta\mathbf{v} \quad (3)$$

(which means that K basically constitutes a measure of the compressibility of the perturbations), we can write the resulting dispersion relation in a form that closely resembles the incompressible dispersion relation of BH:

$$\left(\tilde{\sigma}^2 - \frac{k_r K}{k^2} \sigma^2 \right) \frac{k^2}{k_z^2} \tilde{\sigma}^2 + \Omega^2 \tilde{\sigma}^2 - 4\Omega^2 k_z^2 v_{Az}^2 - 2\Omega \sigma v_{A\phi} v_{Az} k_z K = 0; \quad (4)$$

where $k = |\mathbf{k}|$, $\mathbf{v}_A = \mathbf{B} / \sqrt{\mu_0 \rho}$ denotes the Alfvén speed and $\tilde{\sigma}^2 \equiv \sigma^2 + k_z^2 v_{Az}^2$. The form (4) of the dispersion relation explicitly demonstrates the dependence on the compressibility. The expression for K turns out to be

$$K = \frac{\tilde{\sigma}^2 \sigma^2 k_r - 2\Omega \sigma k_z^3 v_{A\phi} v_{Az}}{\tilde{\sigma}^2 (\sigma^2 + k_z^2 C_{\text{eff}}^2) + \sigma^2 k_z^2 v_{A\phi}^2}, \quad (5)$$

where σ is one of the roots of Eq. (4). In contrast to what one may expect from its definition in Eq. (3), Eq. (5) shows K does not couple the modes δv_r and δv_ϕ . In the incompressible limit $C_{\text{eff}} \rightarrow \infty$, we have $K = 0$ and indeed recover the dispersion relation of BH.

The value of C_{eff} is determined by the internal energy equation. In the one-temperature approximation suitable, e.g., for protoplanetary discs, it reads:

$$\frac{\partial e}{\partial t} + \nabla \cdot (e\mathbf{v}) = -p \nabla \cdot \mathbf{v} - \nabla \cdot \mathbf{F}, \quad (6)$$

with the radiative flux vector \mathbf{F} in the flux-limited diffusion approximation

$$\mathbf{F} = -eD \frac{\nabla T}{T}, \quad \text{with} \quad D \equiv 4 \frac{aT^4}{e} \frac{\lambda c}{\kappa \rho}. \quad (7)$$

Here, κ is the opacity, c the speed of light and λ the flux limiter, which depends on the flux-limited diffusion model one decides to use. In the linear growth phase, λ is a constant, which is due to the fact that we consider a uniform background. This and the uniformity of the other background quantities allows using D as a parameter for our study, which will be designated as the ‘‘coefficient of radiative diffusion’’. Linearising (6) and using $p = (\gamma - 1)e$, as well as the relation $\delta T/T = \delta p/p - \delta \rho/\rho$ we obtain

$$\sigma \delta p = -\rho C_{\text{eff}}^2 \mathbf{i} \mathbf{k} \cdot \delta \mathbf{v}; \quad (8)$$

where C_{eff} is given by the following expression:

$$C_{\text{eff}}^2 = \gamma_{\text{eff}} \frac{p}{\rho}, \quad \text{with} \quad \gamma_{\text{eff}} \equiv \frac{\gamma + k^2 D/\sigma}{1 + k^2 D/\sigma}. \quad (9)$$

We see that in the linear regime, the influence of radiative diffusion can be described by introducing an effective adiabatic index γ_{eff} . Without radiative diffusion ($D = 0$), we have $\gamma_{\text{eff}} = \gamma$, and C_{eff} is just the adiabatic gas sound speed. With D increasing, the effective adiabatic index γ_{eff} is reduced towards the isothermal value $\gamma_{\text{eff}} = 1$ at $D = \infty$. This reduction happens mostly in the regime where the nondimensional diffusion coefficient $k^2 D/\sigma \sim 1$, as can be seen from Fig. 1, where the effective adiabatic index is plotted as a function of D . Thus, in the linear regime, the only effect of radiative diffusion is to make the physical situation more isothermal.

In order to aid comparison with the dispersion relations derived by other authors, we define (following Blaes & Balbus 1994; Blaes & Socrates 2001)

$$\omega \equiv i\sigma, \quad (10a)$$

$$\tilde{\omega}^2 = -\tilde{\sigma}^2, \quad (10b)$$

$$D_{\text{ms}} \equiv \omega^2 - k_z^2 (C_{\text{eff}}^2 + v_{A\phi}^2), \quad (10c)$$

$$D_{\text{BH}} \equiv \frac{k^2}{k_z^2} \tilde{\omega}^4 - \Omega^2 \tilde{\omega}^2 - 4\Omega^2 k_z^2 v_{Az}^2; \quad (10d)$$

and write Eq. (4) in an alternative way as

$$D_{\text{ms}} D_{\text{BH}} - k_z^2 v_{A\phi}^2 v_{Az}^2 (k^2 \tilde{\omega}^2 + 3k_z^2 \Omega^2) - \frac{k_r^2}{k_z^2} \tilde{\omega}^2 \omega^4 = 0. \quad (11)$$

In the appropriate limits our dispersion relation is consistent with that of other authors, like for example the two fluid dispersion relation of Blaes & Balbus (1994) in the limit of $D \rightarrow 0$ and zero coupling, or the resistive dispersion relation of Sano & Miyama (1999) in the limit $D \rightarrow 0$ and zero resistivity.

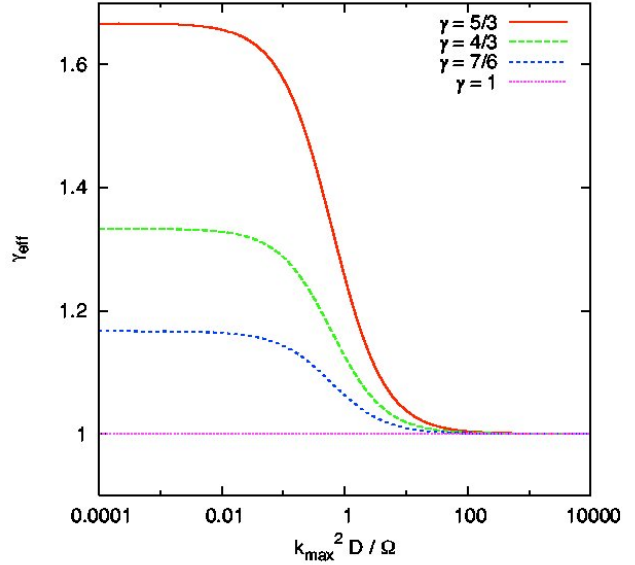


Figure 1. Effective adiabatic index γ_{eff} as a function of $k_{\text{max}}^2 D/\Omega$, where k_{max} is the wavenumber of the fastest growing mode. In this plot, the azimuthal Alfvén speed is taken equal to the isothermal sound speed, $v_{A\phi}^2 = p/\rho$ (the global features of this plot are not sensitive to this particular choice).

Blaes & Socrates (2001) considered the case of a radiation-dominated disc where matter and radiation interact only by momentum exchange and are, therefore, at different temperatures, while we consider the opposite limit where matter and radiation are closely coupled via emission and absorption processes, and are therefore at the same temperature. In the appendix a more general dispersion relation is provided, from which both the Blaes & Socrates dispersion relation and the one given in Eq. (4) can be derived.

2.2 Eigenfunctions

The corresponding eigenfunctions in terms of the radial velocity perturbation δv_r are given by the following formulae:

$$\delta \rho = -i\rho \frac{K}{\sigma} \cdot \delta v_r, \quad (12a)$$

$$\delta v_\phi = \frac{\sigma}{2\Omega k_z^2} \left(k^2 \frac{\tilde{\sigma}^2}{\sigma^2} - k_r K \right) \cdot \delta v_r, \quad (12b)$$

$$\delta v_z = \frac{K - k_r}{k_z} \cdot \delta v_r, \quad (12c)$$

$$\delta p = -i\rho C_{\text{eff}}^2 \frac{K}{\sigma} \cdot \delta v_r, \quad (12d)$$

$$\delta B_r = i \frac{k_z B_z}{\sigma} \cdot \delta v_r, \quad (12e)$$

$$\delta B_\phi = i \left\{ \frac{k_z B_z}{2\Omega} \left(\frac{k^2 \tilde{\sigma}^2}{k_z^2 \sigma^2} - \frac{k_r K}{k_z^2} - 3 \frac{\Omega^2}{\sigma^2} \right) - \frac{K B_\phi}{\sigma} \right\} \cdot \delta v_r, \quad (12f)$$

$$\delta B_z = -i \frac{k_r B_z}{\sigma} \cdot \delta v_r. \quad (12g)$$

Using once more the relation $\delta T/T = \delta p/p - \delta \rho/\rho$, we can derive the following expression for the temperature perturbation:

$$\frac{\delta T}{T} = \frac{\gamma - 1}{1 + k^2 D/\sigma} \frac{\delta \rho}{\rho}. \quad (13)$$

As said, radiative diffusion tends to make the situation more isothermal, and thus for $D \rightarrow \infty$ we have $\delta T \rightarrow 0$, as is to be expected.

2.3 Change of growth rates due to compressibility and radiative diffusion

In order to quantify the effects of a finite compressibility and radiative diffusion on the growth rates, we first look at the vertical modes ($k_r = 0$) which have the largest growth rates. By differentiating the dispersion relation (4) with respect to C_{eff}^{-2} , we find for the change of the growth rate σ with respect to a change in the effective sound speed:

$$\frac{1}{\sigma} \left(\frac{d\sigma}{dC_{\text{eff}}^{-2}} \right)_{C_{\text{eff}}=\infty} = -\frac{2k^2 v_{\Lambda z}^2 / \tilde{\sigma}^2}{1 + 2\tilde{\sigma}^2 / \Omega^2} v_{\Lambda \phi}^2. \quad (14)$$

From this result we conclude that for vertical modes the effect of a nonzero compressibility leads to a decrease of the growth rates in the presence of a nonzero azimuthal field. For the fastest growing mode, which, for $C_{\text{eff}} = \infty$, has a growth rate $\sigma_{\text{max}} = 3/4 \Omega$ with wavenumber $k_{\text{max}} = (\sqrt{15}/4) \Omega / v_{\Lambda z}$, this means that the change $\Delta \sigma_{\text{max}}$ in the growth rate as compared to the incompressible case $C_{\text{eff}} = \infty$ is approximately:

$$\frac{\Delta \sigma_{\text{max}}}{\sigma_{\text{max}}} \approx -\frac{1}{5} \frac{v_{\Lambda \phi}^2}{C_{\text{eff}}^2}. \quad (15)$$

The relative dampening of the growth rates is, thus, in this case of the order of $O(v_{\Lambda \phi}^2 / C_{\text{eff}}^2)$.

Curiously, if we consider non-vertical modes ($k_r \neq 0$) and a vanishing azimuthal field, we discover the opposite. In this case we find by an analogous analysis:

$$\frac{1}{\sigma} \left(\frac{d\sigma}{dC_{\text{eff}}^{-2}} \right)_{C_{\text{eff}}=\infty} = \frac{k_r^2}{2k_z^2} \frac{\tilde{\sigma}^2 \sigma^2 / k_z^2 \Omega^2}{1 + 2k^2 \tilde{\sigma}^2 / k_z^2 \Omega^2}. \quad (16)$$

The corresponding shift of the maximum growth rate becomes:

$$\frac{\Delta \sigma_{\text{max}}}{\sigma_{\text{max}}} \approx \frac{27k_r^2}{240k^2} \frac{v_{\Lambda}^2}{C_{\text{eff}}^2}. \quad (17)$$

This effect should not be considered too important, because the growth of the MRI will be dominated by the fastest growing modes, which are the vertical ones. In both cases considered, radiative diffusion contributes a fraction of $(\gamma p/\rho)/C_{\text{eff}}^2 - 1 = \gamma/\gamma_{\text{eff}} - 1$ to the total shift in the growth rates.

The critical wavelength, which is obtained by setting $\sigma = 0$ in the dispersion relation, is the same as in the non-radiative case. This means that radiative diffusion will generally not affect the regime in which the MRI may possibly operate. One should bear in mind however, that not the linear analysis, but only numerical simulations, can provide us with the answers if, in a given situation, the turbulence that is initiated by the MRI will be sustained for a long period of time and how effectively it transports angular momentum.

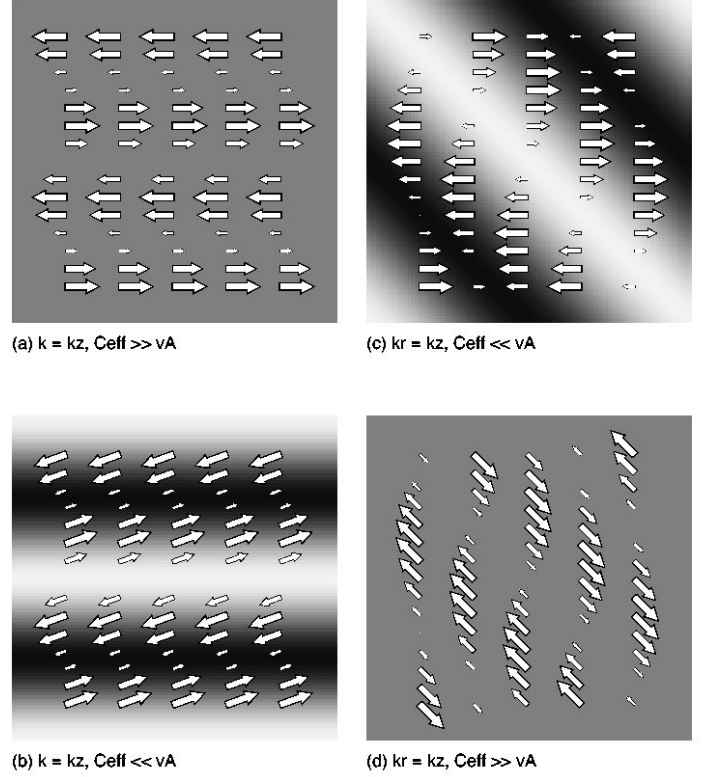


Figure 2. Sketch of the MRI eigenmodes. Plotted is the density perturbation $\delta \rho$ (grayscale) and the velocity perturbation $\delta \mathbf{v}$ (arrows) in the r - z plane. The plots on the left show the case of a vertical mode in the presence of a background azimuthal magnetic field; where (a) corresponds to the incompressible case, while (b) is for finite compressibility. The plots on the right show the case of a nonvertical mode with $k_r = k_z$ where no azimuthal magnetic field is present. Here, (c) corresponds to the case of maximum compressibility and (d) to the incompressible case.

For example, recent results show that in zero-net flux shearing box calculations this depends critically on the value of the magnetic Prandtl number (Fromang et al. 2007).

To summarise, radiative diffusion changes nothing fundamental regarding the growth of the MRI. This is because the radiative effects enter only via the effective adiabatic index γ_{eff} and, thus, change the compressibility, but nothing else. This statement, that the growth of the MRI under the influence of radiative diffusion can be characterised by an effective sound speed, remains true also if we drop the one-temperature approximation (cf. the appendix).

In gas-pressure dominated discs, the growth rates will never be dramatically changed by radiative diffusion, since the variation in C_{eff}^2 covers only a factor of γ . This is different from the situation encountered in a radiation dominated disc, where the analog of C_{eff}^2 may vary greatly. In the presence of a strong enough azimuthal field, the growth rates may thus be severely reduced (cf. the appendix and the paper of Turner et al. 2002).

In order to understand the change of the growth rates due to radiative diffusion in a qualitative manner, let us consider two cases: First, the case of a vertical mode ($\mathbf{k} = k_z \mathbf{e}_z$)

in the presence of an azimuthal field. In the incompressible limit ($C_{\text{eff}} \rightarrow \infty$), the motion of the fluid is confined to the plane perpendicular to the perturbation wavevector, so that $\delta v_z = 0$ (Fig. 2 (a)). When the compressibility is nonzero, the Lorentz force due to the azimuthal magnetic field causes a fluid flow in the vertical direction (Fig. 2 (b)). The higher the compressibility (and the smaller therefore the gas pressure), the more vertical will the velocity vector become. This in turn makes the buildup of the magnetic field less effective, resulting in a smaller growth rate. Radiative diffusion increases the compressibility, and therefore decreases the growth rate.

Next consider the case of a nonvertical mode ($k_r \neq 0$), with no background azimuthal field. If we now start with the limit of maximum compressibility ($C_{\text{eff}} = 0$), we have $\delta v_z = 0$ (Fig. 2 (c)), since the z -component of the Lorentz force vanishes. When now increasing C_{eff} , the gas pressure will act to push the velocity vector into the plane perpendicular to the perturbation wavevector, this effect becoming stronger and stronger as the compressibility is further decreased (Fig. 2 (d)). Therefore, this time *increasing* the compressibility makes the buildup of the magnetic field more effective, which means that the growth rate increases due to radiative diffusion.

When considering the general case of a nonvertical mode in the presence of a nonzero azimuthal field, both effects are present and the result will be either an increase or a decrease of the growth rate, depending on the strength of the azimuthal field and the direction of the perturbation wavevector.

3 NUMERICAL SIMULATIONS

In this section we investigate the growth of the MRI using the appropriate numerical tools. Here we especially aim at a verification of these numerical tools by a comparison to the analytical results derived above. After discussing the numerical scheme we will present the results of the numerical simulations of the MRI.

3.1 Numerical approach

The investigation of the analytical results using a numerical method is clearly not very demanding in this case owing to the fact that the analytical model is restricted to the linear growth phase. Here we decided, however, for a scheme, which is well adapted to high Mach-number turbulence simulations, because we are also interested in more general accretion disc simulations including radiation transport. One of the most important constraints for a numerical scheme used for compressible turbulence simulations is the correct handling of sharp discontinuities. Here we use a second order finite volume scheme based on the work by Kurganov et al. (2001) for the hyperbolic part of the system of equations. This is a central conservative scheme for the solution of equations of the form:

$$\frac{\partial \mathbf{u}}{\partial t} + \nabla \cdot \mathbf{F}(\mathbf{u}) = 0. \quad (18)$$

It does not require a Riemann solver and a characteristic decomposition. This scheme was extended by a constrained transport description for the magnetic field (see,

e.g., Balsara & Spicer 1999; Londrillo & Del Zanna 2000) by which we assure the solenoidality of the magnetic field. This method uses the hyperbolic fluxes to compute electric fields on a staggered grid. These are then used to evolve the magnetic induction, the components of which are also given on a (different) staggered grid. The stability of the code and its capability to resolve steep gradients without introducing artificial oscillations have been proven, e.g., in Kissmann (2006).

Being interested in the evolution of the gas under the influence of radiation transport we also have to deal with the corresponding source terms to the energy equation. These were implemented using two alternative approaches. In the first approach we included the diffusive radiation transport explicitly in the scheme, whereas we used an implicit solver for the second method. This dual approach is motivated by the fact that we are interested in being able to cross-check the two different methods.

For the implicit implementation of the source terms we split the evolution of the radiation from the evolution of the hyperbolic part of the system of equations:

$$e^{(*)} = e^{(n)} + \left(\frac{\partial e}{\partial t} \right)_{\text{hyp}} \quad (19)$$

$$e^{(n+1)} = e^{(*)} + \left(\frac{\partial e}{\partial t} \right)_{\text{rad}} \quad (20)$$

where we evolve the radiation transport step using a parallel ω -Jacobi matrix solver. The ω -Jacobi method is very similar to the method of successive overrelaxation (SOR). It has the advantage that it is simple to implement and very easy to parallelise. We have also a multigrid method available, in case that the ω -Jacobi solver should prove insufficient for high-resolution simulations.

Having an implicit solver for the radiation transport is of special importance with regard to future applications. That is for high resolution simulations with strong radiation transport the time-step of an explicit scheme would become prohibitively small, whereas an implicit solver would only be limited by the Courant condition (see Courant et al. 1928) for the hyperbolic part of the system.

Our second implementation is nonetheless of explicit form, because we wanted to have a completely different method at hand to be able to compare it to the implicit scheme for more general simulations for which no analytical solution is available. For this purpose we extended the flux-function for the energy equation by:

$$\mathbf{F}^{\text{Rad}} = -\frac{e}{T} D \left(\frac{\partial T}{\partial x} \mathbf{e}_x + \frac{\partial T}{\partial y} \mathbf{e}_y + \frac{\partial T}{\partial z} \mathbf{e}_z \right) \quad (21)$$

Since the flux functions are only needed at the cell faces the occurring gradients are easily computed as can be seen from the example of the x -component:

$$F_{x,i+1/2,j,k}^{\text{Rad}} = -\frac{e}{T} D \left(\frac{T_{i+1,j,k} - T_{i,j,k}}{\Delta x} \right) \quad (22)$$

This scheme proved to be stable for:

$$\Delta t < \frac{\Delta x^2}{8D} \frac{\rho T / e}{\gamma - 1} \quad (23)$$

In the following section we will show that both implementations for the radiation transport are well-behaved, yielding correct result when applied to the analytical problem at

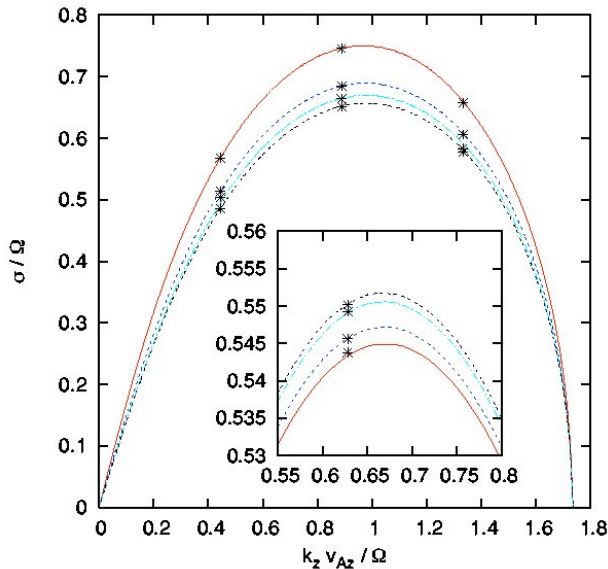


Figure 3. MRI growth rates obtained with the implicit solver. Plotted are the analytical solutions for various cases, together with corresponding data points obtained by numerical simulations. The curves in the main part of the graphic are for vertical modes ($k_r = 0$), where the growth rates are reduced by radiative diffusion. From top to bottom, they represent the following cases, $B_\phi = D = 0$; $B_\phi = 20B_z, D = 10^{-5}$; $B_\phi = 20B_z, D = 10^{-4}$; $B_\phi = 20B_z, D = 1$. The vertical magnetic field in terms of the plasma beta, $\beta = 2\mu_0 p / B^2$, is chosen such that $\beta = 400$, which means that $v_{Az} / \sqrt{p/\rho} \simeq 0.1$. The inset shows simulation results for nonvertical modes with no azimuthal magnetic field, where radiative diffusion increases the growth rates. We chose $k_r = k_z$, $B_\phi = 0$ and B_z such that $v_{Az} = \sqrt{p/\rho}$. From bottom to top, we have $D = 0$, $D = 10^{-5}$, $D = 10^{-4}$, $D = 1$. Although the difference in the growth rates is only small for the latter case, it is accurately reproduced by our numerical code.

hand. Thus, they can be used for future simulations of more complex radiation transport phenomena.

3.2 Growth rates

For our numerical simulations, we use the shearing box approximation (see, e.g., Hawley et al. 1995). In order to compare the analytical growth rates of the MRI to the results from our numerical code, we perform simulations of single MRI eigenmodes. Since only variations in the radial and in the z -directions have to be taken into account, it is sufficient to use a 2D model. We set up the problem using the eigenfunctions as given by (12). The size of the computational domain is $[-0.5, 0.5] \times [-0.5, 0.5]$ (x - and z -direction respectively) with a typical resolution of 64×256 cells. Initially we set $\Omega = 10^{-3}$, density $\rho = 1$ and pressure $p = 10^{-6}$. The simulations were performed for different wavenumbers and for various strengths of magnetic field and radiative diffusion coefficient (for the explicit values see in the figures).

The results are plotted in Figs. 3 and 4 for the implicit and the explicit implementation of the source terms, respectively, together with the corresponding analytical solution. In the simulations with the explicit scheme a constant diffusion coefficient was used [cf. Eq. (21)], while in

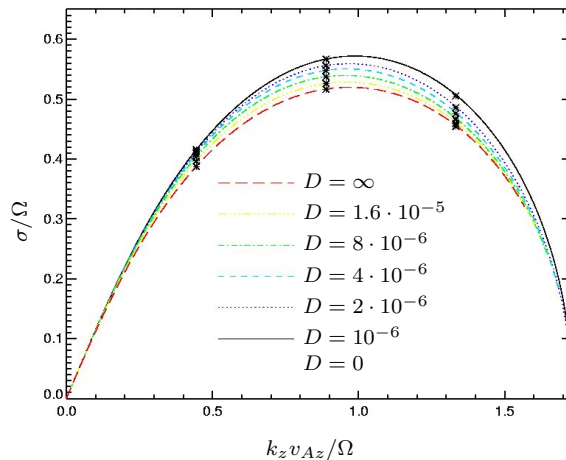


Figure 4. Comparison of the numerical growth rates (black crosses) to the analytical model results (full lines). Here we show the data from the simulations with the explicit numerical implementation of the radiation transport terms. All simulations have $B_\phi = 25B_z$ and a vertical magnetic field corresponding to a plasma beta $\beta = 400$. The curve for $D = \infty$ has been inserted to show the maximum possible change in the growth rates.

the simulations with the implicit scheme, the full radiation transport was done as prescribed by Eq. (7), with $\lambda = 1/3$ and constant opacity κ . The data points nicely match the analytical prediction, thereby confirming both the validity of the numerical scheme and the analytical calculation. In particular it is evident that both implementations of the radiation transport are in good agreement to the analytical predictions. Therefore, we can use both methods to simulate more complex situations in the future giving us the good opportunity to have two different methods to be applied to the same problem. Thus, it will be easier to decide if observed effects might be due to some numerical problem.

3.3 Saturation level

In order to study the impact of radiation transport on the saturation level of the MRI, we switch to a 3D representation of the shearing box with a computational domain $[-0.5, 0.5] \times [0, 4] \times [-0.5, 0.5]$. Concerning the values of ρ, p, Ω we use a similar setup as in the 2D simulations described in the previous section. We choose an initially vertical magnetic field corresponding to a plasma beta of $\beta = 400$ in all simulations. Instead of prescribing eigenfunctions, we initialise the problem with random velocity and pressure perturbations of order 10^{-6} .

The strength of the angular momentum transport is described by the α -parameter (Shakura & Syunyaev 1973). In our simulations, it is measured according to the following prescription:

$$\alpha = \langle T_R + T_M \rangle / p_0, \quad (24)$$

where p_0 is the initial gas pressure, $T_R = \rho \delta v_r \delta v_\phi$ denotes the Reynolds stress and $T_M = -\delta B_r \delta B_\phi$ is the Maxwell stress. The angular brackets $\langle \dots \rangle$ indicate a spatial average. We also use the dimensionless stresses α_R and α_M defined

Table 1. Time- and space-averaged quantities from 3D shearing box simulations performed with our code. In all of the simulations $B_\phi = 0$. In the first three lines, only the resolution is varied, while the last three lines show the dependence on the strength of radiative diffusion. Averages were taken over 10 to 40 orbits.

Resolution	D	E_{mag}/p_0	α	α_M	α_R
32x64x32	1	0.400	0.278	0.248	0.044
128x256x128	1	0.505	0.299	0.279	0.036
64x128x64	1	0.337	0.226	0.195	0.031
64x128x64	0	1.007	0.719	0.599	0.119
64x128x64	10^{-5}	0.358	0.244	0.210	0.034
64x128x64	1	0.337	0.226	0.195	0.031

as

$$\alpha_R = \langle T_R \rangle / p_0, \quad \alpha_M = \langle T_M \rangle / p_0. \quad (25)$$

Note that with this definitions in general we will have $\alpha \neq \alpha_R + \alpha_M$. Due to the fact that in our simulations the magnetic field possesses a net flux, the resulting α is quite large, $\alpha \gtrsim 0.1$.

In order to check if there exists a trend for the turbulent activity with different resolution, we performed three runs where the resolution was successively doubled. Fig. 5 shows the time evolution of the magnetic energy and the α -parameter for this runs. In Table 1 long-term averages of this quantities as well as of the Maxwell and Reynold stresses can be found. The results displayed in Fig. 5 and Tab. 1 indicate no net trend for the change of the saturation level with resolution (the first three lines in the table).

As we have seen, the analytical calculation predicts that radiative diffusion modifies the MRI growth rates. The question if the saturation level of the MRI-induced turbulence is also changed by radiative effects can only be answered by numerical simulations. We have performed simulations with varying radiative diffusion coefficient, where we picked a resolution of 64x128x64. The results show a moderate decrease of the turbulent activity with increasing radiative diffusion coefficient D , see last 3 entries in Tab. 1. A qualitative explanation for this is given below.

We have also performed additional simulations with the ZEUS code in order to check this result using a different numerical scheme. We used the same setup concerning ρ, p, Ω as in the simulations done with our code. The strength of the constant vertical magnetic field was taken as corresponding to a plasma beta of $\beta = 800$. We performed simulations with and without azimuthal magnetic field B_ϕ , using different resolutions (see Table 2). In Fig. 6, the magnetic energy is plotted for the high resolution simulations. As has already been stated in the introduction, it is known that the outcome of an MRI simulation does depend on numerical issues such as the resolution or the numerical magnetic Prandtl number of the code (Fromang & Papaloizou 2007). Indeed, if we compare for example the simulations in lines 3 and 4 of Tab. 1 with the corresponding simulations done with the ZEUS code, lines 5 and 6 of Tab. 2, the ratio of the saturation levels in the case of the ZEUS code turns out to be about a factor of two smaller than in the simulations done with our code. We have checked that this fact remains true even if we choose the same initial plasma beta

Table 2. 3D shearing-box simulations performed with ZEUS. In some of the simulations, a non-zero constant B_ϕ was used, leading to a higher saturation level. Averages were taken from 10 to 40 orbits.

Resolution	D	$\frac{B_\phi}{B_z}$	E_{mag}/p_0	α	T_M	T_R
32x64x32	0	0	0.398	0.248	0.210	0.038
32x64x32	1	0	0.245	0.146	0.123	0.023
32x64x32	0	20	2.557	1.125	0.983	0.141
32x64x32	1	20	1.542	0.577	0.498	0.079
64x128x64	0	0	0.552	0.335	0.288	0.047
64x128x64	1	0	0.392	0.218	0.187	0.031
64x128x64	0	20	2.474	1.137	1.006	0.131
64x128x64	1	20	2.315	1.075	0.938	0.137

as in the runs with our code. Despite these issues, all runs unambiguously show that the saturation level decreases with increasing radiative diffusion.

A plausible explanation for the phenomenon of the reduction of the saturation level due to radiative diffusion can be given as follows: In the case of an initial magnetic field with nonzero net flux, the turbulence in the saturated state is still partially pumped by the two-channel mode (the vertical mode with the longest wavelength that fits into the box). The channel mode reappears every few orbits; a manifestation of this are the oscillations that can be seen in the time evolution of the magnetic energy and the α -parameter (see, for example Sano & Inutsuka 2001). In Sec. 2.3 we have seen that radiative transport tends to decrease the growth rates of vertical modes by effectively increasing the compressibility of the fluid and thus making it easier for the Lorentz force to push the velocity vectors out of the r - ϕ plane. Therefore it is to be expected that radiative transport, by decreasing the growth rate of the recurrent channel mode, acts to reduce the turbulent activity.

3.4 Temperature distribution

For the full 3D simulation the influence of the radiation transport can also be visualised by the temperature distribution. This is shown in Fig. 7 for a similar setup as described in the previous section. Here we used an extent of the computational domain of $[-0.5, 0.5] \times [0, 6] \times [-0.5, 0.5]$ with the same spatial resolution of 64x128x64. The z -component of the magnetic induction was initialised with $\beta = 800$, and we chose $B_\phi = 20B_z$. We followed the evolution for several orbits. In Fig. 8 we show the distribution in the density - thermal energy plane for one simulation without and one with radiative transport. Apparently the plasma gets more isothermal when radiation transport is present – for a fully isothermal simulation the thermal energy would depend linearly on the density, thus, yielding a line in this plot. This fact also becomes apparent, when comparing the results for the temperature distribution function.

This is done in Fig. 7 for the same simulations. Here, the temperatures are normalised to the initial temperature (that is, initially we had a delta-peak at $T = 1$). The shift of the distribution functions with regard to the initial temperature results from the heating by (numerical) viscosity and resistivity. Obviously the distribution for the disc with radiation transport is considerably narrower. Note, however,

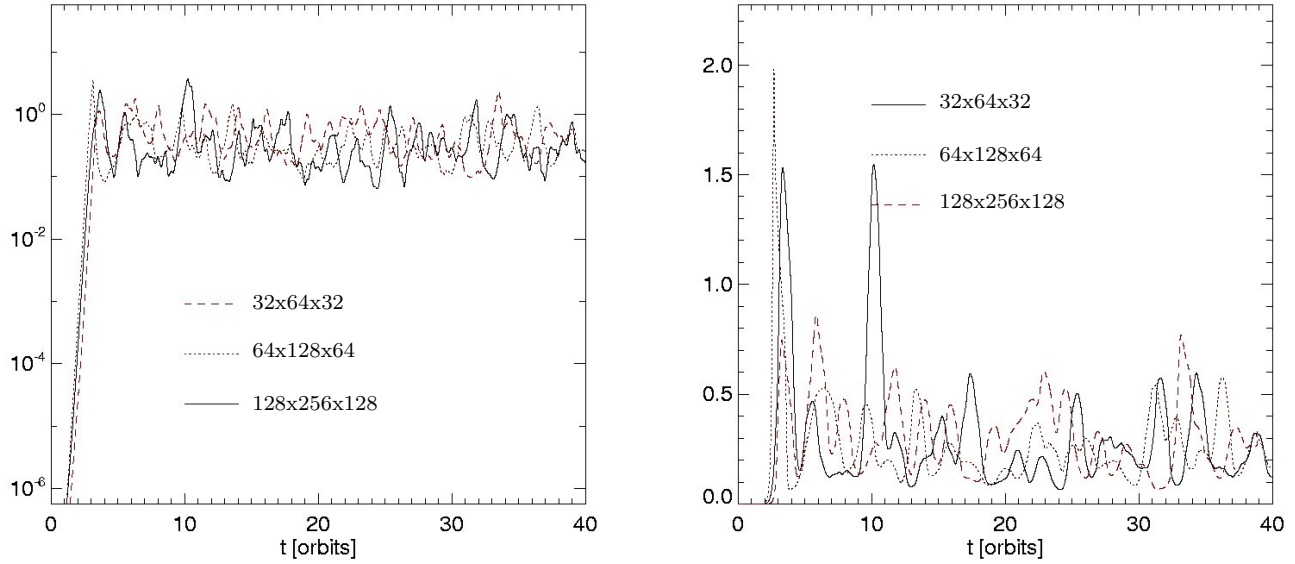


Figure 5. Resolution dependence of the turbulent activity on the numerical resolution. The left and right panels show the time evolution of the perturbed magnetic energy and the alpha parameter, respectively. In case of the alpha parameter the curves have been smoothed over 1 orbit. When considering long-term averages of these quantities, there appears to be no trend with varying resolution.

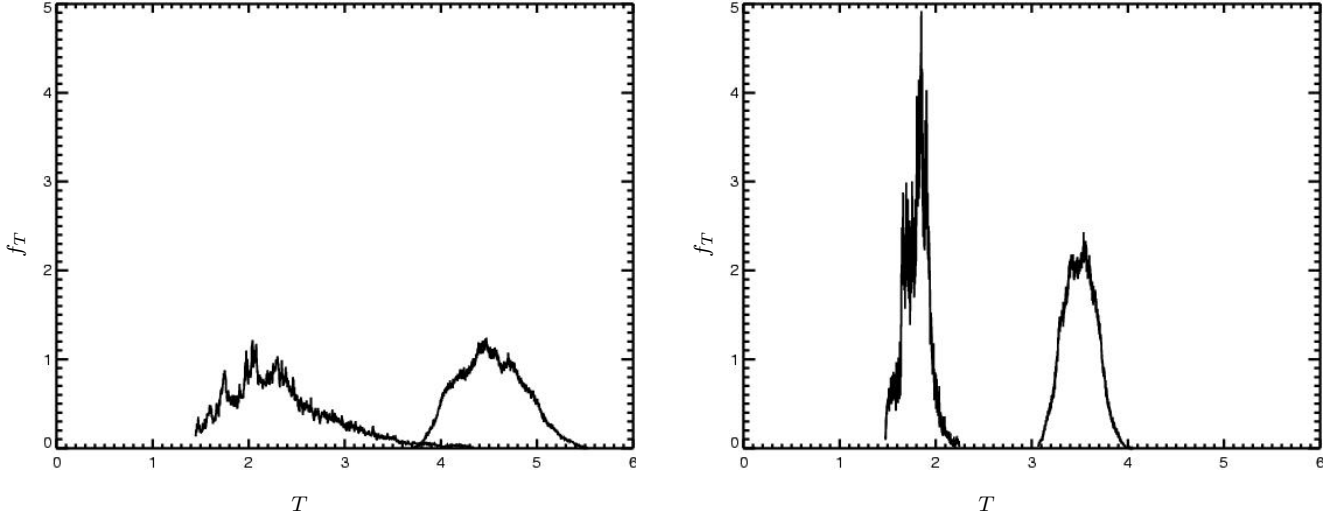


Figure 7. Temperature distribution for two 3D simulations without radiation transport (left) and with radiative transport, $D = 4 \cdot 10^{-5}$ (right). In both plots, the distribution to the left corresponds to $t = 3.5$ orbits, while the right corresponds to $t = 4.1$ orbits. In the case with radiative transport, the width of the distribution function is smaller and the heating occurs less rapidly.

that also for this case the temperature after several orbits differs markedly from the initial temperature. This conclusion is also strengthened by the fact that both distributions are centered at nearly the same temperature. This is due to the fact that the gas is still heated by viscosity and resistivity. In contrast to the case without radiation transport the local temperature enhancements are smoothed out by the radiation transport.

4 DISCUSSION

We analysed the influence of radiation transport on the magnetorotational instability. We started by investigating the linear growth of small disturbances on an underlying constant shear flow. The system under investigation is a magnetised shearing box, where we explicitly retained the compressibility of the gas. Additionally we took radiation transport via flux-limited diffusion into account. For this system we derived a general dispersion relation, which in the appropriate limits can be reduced to several dispersion relations known from the literature.

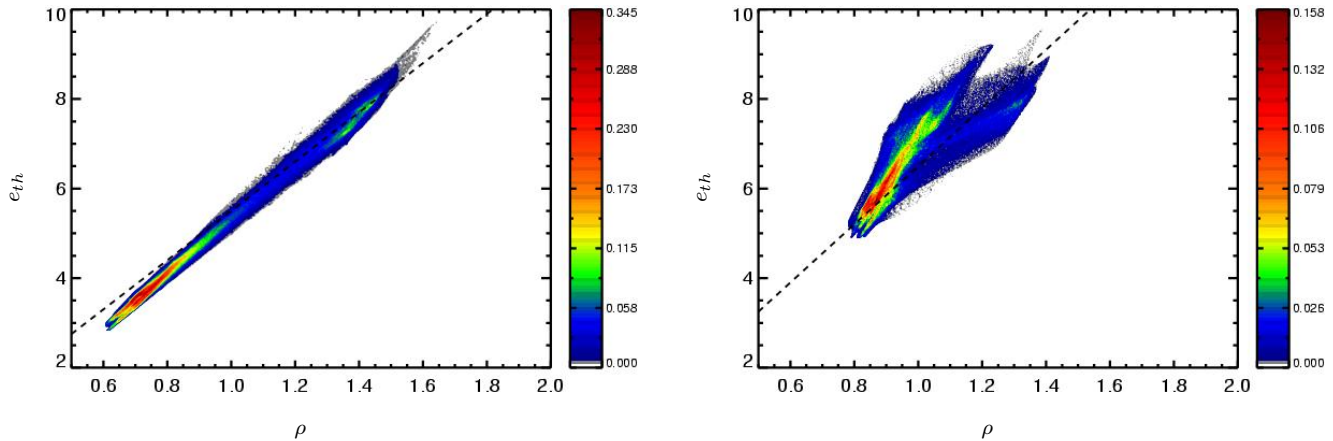


Figure 8. Distribution in the density- thermal energy plane. Values are shown in normalised units. Here we show the distribution function for a simulation without radiative transport (left) and one where we used $D = 4 \cdot 10^{-5}$ (right). Both snapshots are taken at time $t = 4.1$ orbits.

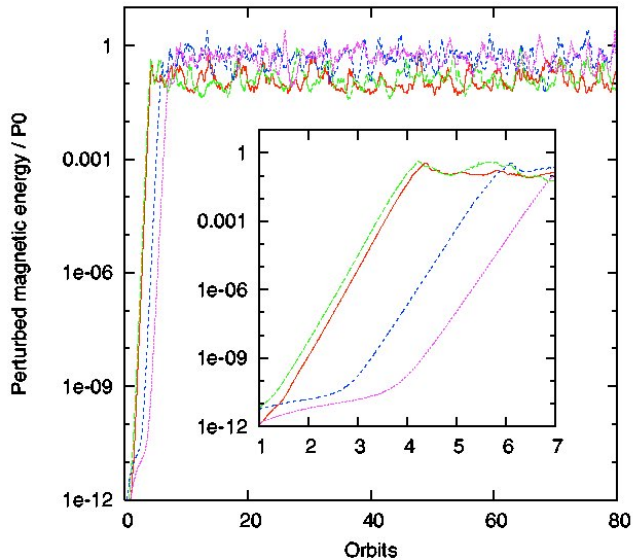


Figure 6. 3D shearing box simulations performed with ZEUS at resolution $64 \times 128 \times 64$. Shown is the perturbed magnetic energy normalised to the initial gas pressure. The solid, dashed, dot-dashed and dotted curves correspond to the combinations $B_\phi = 0/D = 0$, $B_\phi = 0/D = 1$, $B_\phi = 20B_z/D = 0$ and $B_\phi = 20B_z/D = 1$, respectively. In the linear phase, the obtained growth rates are only a few percent smaller than the growth rate of the fastest growing mode that fits in the box, which means that the initial growth is dominated by the fastest growing mode, as is to be expected.

Here, we placed special emphasis on the one-temperature flux-limited diffusion approximation suited for accretion discs not dominated by the radiation. The corresponding dispersion relation can also be derived from the general relation given in the appendix. From this we computed the growth rates for the linear case, which we then also compared to the results from numerical simulations. The excellent agreement between simulations and analytical

prediction not only confirmed the accuracy of the employed numerical schemes but also the correctness of the analytical solution.

This analysis was then further extended by numerical simulations, which also took the non-linear phase of the instability into account. These simulations were done for a more general case, where several modes of the instability were excited in a fully three dimensional setup. There we concentrated on the resulting saturation levels of the turbulence and on the temperature distribution, which is also influenced by the radiation transport.

From our analysis it is apparent that the influence of the radiation transport is a rich phenomenon. It not only weakens the magnetorotational instability, but can also enhance it in a certain parameter regime. This shows that radiation transport – even in the one-temperature flux-limited diffusion limit – does not simply act as a dissipative process like viscosity and resistivity. Another difference between these processes is that the latter can completely suppress the instability, whereas radiation transport can only weaken it. This is due to the fact that a diffusive radiation transport only smooths the temperature, whereas the other dissipative processes directly act onto either velocity or magnetic field fluctuations. Thus, we have, for strong radiation transport, approximately an isothermal state of the plasma. This, however, still differs from the use of an isothermal equation of state with the difference arising from the fact that when using an energy equation with γ differing from one, we still have heating due to dissipative processes (either physical or numerical). Thus, the effect of radiation transport is just to smooth out the local peaks of heat appearing due to local dissipation.

This picture will probably become different, when investigating the MRI in an open box instead of the periodic shearing box. The future task will, thus, be the investigation of a stratified shearing box, where we can allow for outgoing radiation in the halo of the disc. This way even a nearly isothermal core of the disc might occur, which might then be compared to simulations using an isothermal equation of state. Here, however, we have restricted ourselves to the in-

vestigation of the local shearing box, since only this can be approached by analytical means.

Acknowledgements

This research has been supported in part by the Deutsche Forschungsgemeinschaft DFG through grant DFG Forschergruppe 759 “The Formation of Planets: The Critical First Growth Phase”. Computational resources were provided by the High Performance Computing Cluster of the University of Tübingen and in the project hbo25 by the Forschungszentrum Jülich. We thank the anonymous referee for providing valuable suggestions that helped to improve the paper.

APPENDIX A: GENERAL DISPERSION RELATION

In this appendix, we provide the general dispersion relation by including the radiation energy equation and dropping the one-temperature approximation. This means that in the momentum equation (1b), we have to replace ∇p by $\nabla p + \lambda \nabla E$, where E denotes the radiation energy density. As in Eq. (7) λ denotes the flux limiter, which is constant in the linear growth phase due to the constant background. The effect of this is that in the linearised momentum equation (2b), we should now define the effective sound speed C_{eff} as

$$C_{\text{eff}}^2 \equiv \frac{\delta p}{\delta \rho} + \lambda \frac{\delta E}{\delta \rho}. \quad (\text{A1})$$

To determine it, we need the internal energy equation and the radiation energy equation:

$$\frac{\partial e}{\partial t} + \nabla \cdot (e \mathbf{v}) = -p \nabla \cdot \mathbf{v} - \kappa_{\text{P}} \rho (4\pi B - cE), \quad (\text{A2a})$$

$$\frac{\partial E}{\partial t} + \nabla \cdot (E \mathbf{v}) = -\frac{E}{3} \nabla \cdot \mathbf{v} + \kappa_{\text{F}} \rho (4\pi B - cE) - \nabla \cdot \mathbf{F}. \quad (\text{A2b})$$

Here, B denotes the Planck function and κ_{P} the Planck mean opacity. The terms containing κ_{P} describe the coupling of the gas to the radiation via emission and absorption. The radiative flux vector now reads

$$\mathbf{F} = -\frac{\lambda c}{\kappa_{\text{F}} \rho} \nabla E, \quad (\text{A3})$$

where κ_{F} is the flux-mean total opacity. We define

$$\alpha_{\text{P}} \equiv \frac{\kappa_{\text{P}} \rho c}{\sigma} \quad \text{and} \quad \alpha_{\text{F}} \equiv \frac{k^2}{\sigma} \frac{\lambda c}{\kappa_{\text{F}} \rho}, \quad (\text{A4})$$

The dimensionless quantity α_{P} gives the rate at which radiation and matter are thermally coupled with respect to the growth rate of the instability while α_{F} constitutes a non-dimensional diffusion coefficient. We assume that in the equilibrium the gas temperature T_{g} and radiation temperature T_{r} defined by $E = aT_{\text{r}}^4$ are equal: $T_{\text{g}} = T_{\text{r}} \equiv T$ and $\frac{4\pi B}{c} = aT^4$. Now the linearised equations corresponding to Eqs. (A2) become:

$$\delta p = \gamma \frac{p}{\rho} \delta \rho - (\gamma - 1) \alpha_{\text{P}} E \left(4 \frac{\delta T_{\text{g}}}{T} - \frac{\delta E}{E} \right), \quad (\text{A5})$$

$$\delta E = \frac{4E}{3\rho} \delta \rho + \alpha_{\text{P}} E \left(4 \frac{\delta T_{\text{g}}}{T} - \frac{\delta E}{E} \right) - \alpha_{\text{F}} \delta E; \quad (\text{A6})$$

From these linearised equations we find after some algebra

$$\frac{\delta p}{\delta \rho} = \frac{(1 + \alpha_{\text{P}} + \alpha_{\text{F}}) \left(\gamma + \frac{4E}{3e} \right) - \frac{4E}{3e} (1 - 3\alpha_{\text{P}}) (1 + \alpha_{\text{F}})}{1 + \alpha_{\text{P}} + \alpha_{\text{F}} + 4\alpha_{\text{P}} \frac{E}{e} (1 + \alpha_{\text{F}})} \frac{p}{\rho}, \quad (\text{A7a})$$

$$\frac{\delta E}{\delta \rho} = \frac{1 + 4\alpha_{\text{P}} \left(\gamma - 1 + \frac{4E}{3e} \right)}{1 + \alpha_{\text{P}} + \alpha_{\text{F}} + 4\alpha_{\text{P}} \frac{E}{e} (1 + \alpha_{\text{F}})} \frac{E}{\rho}. \quad (\text{A7b})$$

In conclusion, let us look at the limits of gas-pressure dominated and radiation-pressure dominated discs, respectively. In the limit $\alpha_{\text{P}} \rightarrow \infty$, $E/e \rightarrow 0$, suitable for a gas-pressure dominated disc, we get

$$\frac{\delta p}{\delta \rho} = \frac{\gamma + 4 \frac{E}{e} \alpha_{\text{F}}}{1 + 4 \frac{E}{e} \alpha_{\text{F}}} \frac{p}{\rho}, \quad \frac{\delta E}{\delta \rho} = 0; \quad (\text{A8})$$

and in this way recover our Eqs. (9). For the case of a radiation dominated disc where $\alpha_{\text{P}} \rightarrow 0$,

$$C_{\text{eff}}^2 = \frac{\gamma p}{\rho} + \frac{4\lambda E/3\rho}{1 + \alpha_{\text{F}}}. \quad (\text{A9})$$

When using this value for C_{eff} , and setting $\lambda = 1/3$, Eq. (11) becomes identical to the Blaes & Socrates (2001) dispersion relation. The general dispersion relation provided in this appendix, thus, encompasses both the case of a gas-pressure dominated disc, such as a protoplanetary disc, and the opposite extreme of a radiation-pressure dominated system like an accretion disc around a black hole.

REFERENCES

- Armitage P. J., 1998, *ApJ*, 501, L189+
- Balbus S., Hawley J., 1991, *ApJ*, 376, 214
- Balbus S. A., 2003, *ARA&A*, 41, 555
- Balbus S. A., Hawley J. F., 2006, *ApJ*, 652, 1020
- Balsara D. S., Spicer D. S., 1999, *Journal of Computational Physics*, 149, 270
- Blaes O., Hirose S., Krolik J. H., 2007, *ApJ*, 664, 1057
- Blaes O., Socrates A., 2001, *ApJ*, 553, 987
- Blaes O. M., Balbus S. A., 1994, *ApJ*, 421, 163
- Brandenburg A., 2008, *Physica Scripta*, p. 014016
- Brandenburg A., Nordlund A., Stein R. F., Torkelsson U., 1995, *ApJ*, 446, 741
- Courant R., Friedrichs K., Lewy H., 1928, *Math. Ann.*, 100, 32
- Fromang S., Nelson R. P., 2006, *A&A*, 457, 343
- Fromang S., Papaloizou J., 2007, *A&A*, 476, 1113
- Fromang S., Papaloizou J., Lesur G., Heinemann T., 2007, *A&A*, 476, 1123
- Hawley J. F., 2000, *ApJ*, 528, 462
- Hawley J. F., Balbus S. A., Winters W. F., 1999, *ApJ*, 518, 394
- Hawley J. F., Gammie C. F., Balbus S. A., 1995, *ApJ*, 440, 742
- Hirose S., Krolik J. H., Stone J. M., 2006, *ApJ*, 640, 901
- King A. R., Pringle J. E., Livio M., 2007, *MNRAS*, 376, 1740
- Kissmann R., 2006, PhD thesis, Ruhr-Universität Bochum
- Kley W., Crida A., 2008, *A&A*, 487, L9
- Krolik J. H., Hirose S., Blaes O., 2007, *ApJ*, 664, 1045
- Kurganov A., Noelle S., Petrova G., 2001, *SIAM J. Sci. Comput.*, 23, 707

- Levermore C. D., Pomraning G. C., 1981, *ApJ*, 248, 321
Londrillo P., Del Zanna L., 2000, *ApJ*, 530, 508
Miller K. A., Stone J. M., 2000, *ApJ*, 534, 398
Papaloizou J. C. B., Nelson R. P., 2003, *MNRAS*, 339, 983
Pessah M. E., Chan C.-k., Psaltis D., 2007, *ApJ*, 668, L51
Pringle J. E., 1981, *ARA&A*, 19, 137
Sano T., Inutsuka S.-i., 2001, *The Astrophysical Journal Letters*, 561, L179
Sano T., Miyama S. M., 1999, *The Astrophysical Journal*, 515, 776
Shakura N. I., Syunyaev R. A., 1973, *A&A*, 24, 337
Turner N. J., 2004, *The Astrophysical Journal Letters*, 605, L45
Turner N. J., Stone J. M., Krolik J. H., Sano T., 2003, *ApJ*, 593, 992
Turner N. J., Stone J. M., Sano T., 2002, *ApJ*, 566, 148